



Simultaneous reactant accessibility and charge transfer engineering in Co-doped RuO₂-supported OCNT for robust rechargeable zinc-air batteries

Qian Lu^a, Xiaohong Zou^{b,*}, Xixi Wang^c, Liang An^b, Zongping Shao^{d,*}, Yunfei Bu^{a,*}

^a Jiangsu Collaborative Innovation Center of Atmospheric Environment and Equipment Technology, Jiangsu Key Laboratory of Atmospheric Environment Monitoring and Pollution Control, UNIST-NUIST Environment and Energy Jointed Lab, School of Environmental Science and Technology, Nanjing University of Information Science and Technology, Nanjing 210044, PR China

^b Department of Mechanical Engineering, The Hong Kong Polytechnic University, Hung Hom, Kowloon, Hong Kong, China

^c College of Chemical Engineering, Nanjing Tech University, No. 30 South Puzi Road, Nanjing 211816, PR China

^d WA School of Mines: Minerals, Energy and Chemical Engineering (WASM-MECE), Curtin University, Perth, WA 6845, Australia

ARTICLE INFO

Keywords:

Zinc-air batteries

Ru/Co dual-site

Supported electrocatalysts

Reactant accessibility

Charge transfer

ABSTRACT

The sluggish oxygen reduction/evolution reaction (ORR/OER) kinetics greatly limits the application of zinc-air batteries (ZAB). Regarding this, searching for high-efficient electrocatalysts should be emphatically considered, while reactant accessibility and charge transfer on catalysts are the decisive factors for ORR/OER activities. Here we propose the incorporation of excess Co into (101) plane of RuO₂ to form a single-phase material with abundant Ru/Co dual-atom sites on the active (110) surface to simultaneously optimize the charge transfer and reactant accessibility in the electrode reactions, while oxidized carbon nanotube applied as supports for electron transfer. Ru and Co atoms serve as the main ORR and OER catalytic sites respectively, while Ru/Co dual atoms tend to co-adsorb the intermediate *OOH to produce the synergistic effects. As a result, the optimal electrocatalysts achieve an ultralow overpotential gap of 0.67 V in 0.1 M KOH and superior stability over 800 cycles at 10 mA cm⁻² for ZAB.

1. Introduction

Searching high-efficient energy storage and conversion device for renewable new energy is a pressing matter to reduce CO₂ emissions, thus achieving the goal of “carbon neutralization” [1–4]. Among various devices, rechargeable Zn-air battery (ZAB) gains more attraction in recent years based on their high energy density and environmental friendliness [5,6]. For ZAB, constructing highly active oxygen reduction reaction (ORR) and oxygen evolution reaction (OER) electrocatalysts is an urgent matter for facilitating its commercialization process considering the sluggish kinetics of proton-coupled electron transfer (PCET) steps in air cathode [7–9].

The charge transfer rate in the interface of electrolyte/electrocatalyst determines the reaction rate of PCET steps [10]. Generally, ORR and OER require different catalytic sites located near the top of “volcanic curves” owing to distinct rate-determining steps for ORR and OER [11]. Recently, researchers hold the view that interface engineering in hetero-electrocatalyst with dual catalytic sites for ORR and OER can induce unexpected positive effects in charge transfer kinetics, including

synergistic effect [12], strain effect [13], and electron coupling effect [14]. Among various hetero-electrocatalysts, ruthenium oxide and cobalt oxide composites show great promise in achieving excellent ORR/OER activities and even the stabilities owing to the strong electron interaction among Ru-O-Co interfacial atoms [15–19]. For instance, Zhang et al. reported a double-phase coupling strategy to construct the bimetallic RuO₂ and Co₃O₄ for rechargeable ZABs, in which the interfacial Ru-O-Co bonds between two components can induce the modulation of electronic structure and thus offer synergistic effects [20]. Moreover, our group proposed a surface precipitation strategy to deposit sub-1 nm RuO_x clusters on Co₃O₄ porous supports to build abundant Ru-O-Co interfacial bonds for altering the charge density in both RuO_x clusters and Co₃O₄ to promote charge transfer [21]. According to these reports, the interfacial Ru/Co dual atoms that are regarded as highly active catalytic site plays a critical role in synergistically adsorbing the oxygen intermediates, thus regulating the charge transfer kinetics of ORR and OER. Therefore, achieving abundant Ru/Co dual atoms on an active surface can magnify the positive effects of interfacial atoms.

Besides the charge transfer, the diffusion rate of reactants including

* Corresponding authors.

E-mail addresses: xiaohong.zou@polyu.edu.hk (X. Zou), shaozp@njtech.edu.cn (Z. Shao), Yunfei.bu@nuist.edu.cn (Y. Bu).

<https://doi.org/10.1016/j.apcatb.2022.122323>

Received 19 October 2022; Received in revised form 16 December 2022; Accepted 21 December 2022

Available online 26 December 2022

0926-3373/© 2022 Elsevier B.V. All rights reserved.

oxygen, water, and OH⁻ across the depletion layer determines the reaction capacity of ORR and OER process [22–24]. Especially, the oxygen diffusion capacity directly determines the ORR catalytic activity owing to the diffusion-controlled process [25]. Recent work indicates that enhancing the surface area and pore structure can promote the diffusion capacity of reactants owing to the high contact area [26,27]. In addition, Lou et al. reported that the adsorbed H₂O* on the metal site thermodynamically prefers to couple with the reactants including oxygen and OH⁻ species, thus improving the formation rate of subsequent intermediates during ORR and OER process [28]. Meanwhile, the adsorbed H₂O* on catalysts surface can serve as effective proton donors to promote the corresponding PCET steps of ORR and OER [29]. Therefore, enhancing the surface area of active site and content of adsorbed H₂O* on the metal site can facilitate the reactant accessibility for achieving high catalytic activity. To improve the reaction kinetics in air cathode, the reactant accessibility and charge transfer rate on the catalyst's surface should be considered simultaneously [30]. Regarding the above, constructing single-phase Ru/Co bimetallic oxide with a high surface area for exposing active site, abundant Ru/Co dual atom on the active surface, and high content of adsorbed H₂O* on active site is favored for ORR and OER catalytic performance, yet a great challenge.

Herein, we propose a supported electrocatalyst with excess Co-doped RuO₂ nanoparticle anchoring on oxidized carbon nanotube (Co-RuO₂/OCNT) through a solvothermal route. The Co ion is mainly doped into (101) plane of tetragonal RuO₂ to achieve an abundant Ru/Co dual-atom site on the active (110) surface. Moreover, the Co-RuO₂ nanoparticle with an average size of 5.1 nm is evenly supported on OCNT via the defect site, which can further enhance the exposed area of Ru/Co dual-atom site. The adjacent Ru and Co atoms serve as the main OER and ORR catalytic sites, especially co-adsorbs OOH* with a quadrilateral structure to overcome the rate-determining steps of ORR and OER on Co and Ru sites respectively. In addition, the Ru site with abundant adsorbed H₂O* (38.3%) and Co site with rich electrons can also promote the reactants including H₂O, oxygen, and OH⁻ accessibility and break of O=O double bonds respectively owing to the charge redistribution effect, while the OCNT supports provide a fluent channel for fast electron transport. As a proof of concept, optimal Co-RuO₂/OCNT achieves an ultralow ORR/OER overpotential gap of 0.67 V in 0.1 M KOH, which is much lower than RuO₂/OCNT, Co₃O₄/OCNT, and most of reported works. Remarkably, ZABs assembled with Co-RuO₂/OCNT exhibits high peak energy density of 198 mW cm⁻², specific capacity of 790 mAh g_{Zn}⁻¹ at 20 mA cm⁻², and superior cycling stability over 800 cycles at 10 mA cm⁻². We believe that the insights in constructing supported electrocatalyst with abundant dual-metal catalytic sites provides promising directions for engineering highly efficient rechargeable ZAB.

2. Experimental

2.1. Materials

Gas diffusion layer was bought from Changzhou Youteke New Energy Technology Co., Ltd (China). Commercially available multi-walled carbon nanotube (CNT, 97%wt) was obtained from Nanjing Xianfeng Nanomaterial Technology Co., Ltd (China). Co(NO₃)₂•6 H₂O (AR, 98.5%), HNO₃ (GR, 99.0%), Hexamethylenetetramine (AR, 99.0%), isopropanol (AR, 99.5%) and Dimethylformamide (AR, 99.5%) were purchased from Sinopharm Chemical Reagent Co., Ltd (China). KOH (GR, 99.99%) and ZnCl₂ (AR, 99.5%) were acquired from Aladdin Co., Ltd (China). RuCl₃•3 H₂O (GR, 99.99%) was purchased from Alfa Aesar Co., Ltd (America). All reagents were employed without further purification.

2.2. Synthesis of oxidized carbon nanotube

First, 2 g commercial multi-walled carbon nanotube (CNT, 97%wt) was dispersed into 100 mL 4 mol L⁻¹ nitric acid through ultrasonication

treatment. The obtained solution was then treated by reflux condensation at 110 °C for 2 h. Further, vacuum filtration was applied to separate the oxidized CNT from the above-obtained mixture while washing with deionized water for three times to remove the impurities. Finally, the oxidized CNT (OCNT) powder was obtained by vacuum freeze-drying method.

2.3. Synthesis of Co-RuO₂/OCNT

Co-RuO₂/OCNT was synthesized by a simple solvothermal method. First, 0.05 g oxidized CNTs were dispersed into 30 mL N, N-dimethylformamide (DMF) by ultrasonication for 10 min to ensure the uniform dispersion of OCNT. Subsequently, 0.14 g Co(NO₃)₂•6 H₂O, 0.049 g RuCl₃•3 H₂O, and 0.2 g hexamethylenetetramine were added into the above dispersions through ultrasonication for 10 min to achieve their complete dissolution. Further, the mixture was transferred to a Teflon autoclave and treated for 5 h at 160 °C in a bake oven. After cooling to room temperature, the obtained solution was treated by vacuum filtration and washed with deionized water and methanol several times to obtain the catalyst precursor. Subsequently, the catalyst precursor was oven dried for 2 h at 60 °C in a bake oven. Finally, the dried catalyst precursor was annealed at 300 °C in a muffle furnace for 3 h with a heating rate of 5 °C min⁻¹ to obtain the Co-RuO₂/OCNT. For exploring the optimal loads of Co-RuO₂ on OCNT, the high load (Co-RuO₂/OCNT-H) with the addition of 0.20 g Co(NO₃)₂•6 H₂O, 0.070 g RuCl₃•3 H₂O, and 0.3 g hexamethylenetetramine, and the low load (Co-RuO₂/OCNT-L) with the addition of 0.08 g Co(NO₃)₂•6 H₂O, 0.028 g RuCl₃•3 H₂O and 0.1 g hexamethylenetetramine were respectively prepared via above synthesis process. Further, the different doping amounts of Co in RuO₂-supported OCNT were obtained through same procedure, differently, the amount of Co(NO₃)₂•6 H₂O was set as 0.07 g (0.5Co-RuO₂/OCNT), 0.105 g (0.75Co-RuO₂/OCNT), and 0.175 g (1.25Co-RuO₂/OCNT), respectively. In addition, RuO₂/OCNT and Co₃O₄/OCNT were synthesized through the above similar procedure except for replacing the metal salt (0.14 g Co(NO₃)₂•6 H₂O and 0.049 g RuCl₃•3 H₂O) to 0.147 g RuCl₃•3 H₂O and 0.21 g Co(NO₃)₂•6 H₂O respectively.

2.4. Materials characterization

Rigaku Smart Lab was utilized to gain the X-ray diffraction pattern of as-prepared catalysts using Cu Kα radiation (λ = 1.5406 Å, 40 kV and 40 mA) under a scan rate of 10° min⁻¹. Scanning electron microscope and transmission electron microscope were applied to detect the micro-morphology and atomic structure of Co-RuO₂/OCNT using Hitachi S-4800 and FEI Talos F200X respectively. Raman spectra were collected with an excitation laser under 632 nm using a Horiba LabRAM HR spectroscopy. X-ray photoelectron spectroscopy was collected by PHI5000 Versa Probe with Al Kα X-ray source for testing the electronic structure of Co-RuO₂/OCNT, RuO₂/OCNT, and Co₃O₄/OCNT, in which all spectrum was corrected by C 1 s line at 284.8 eV. XPSPEAK software was applied to fit the high-resolution XPS spectrum. The inductively coupled plasma optical emission spectrometer (ICP-OES) was conducted on Varian 720-ES for detecting the mass content of Co and Ru in the KOH electrolyte.

3. Results and discussion

3.1. Synthesis and characterization

The Co-RuO₂/OCNT electrocatalyst was prepared via a simple solvothermal method as illustrated schematically in Fig. 1a. To better disperse the Co-RuO₂ nanoparticle, carbon nanotube supports were first oxidized by HNO₃ to induce extensive defects [31], named OCNT. Further, Co-RuO₂ nanoparticle was in situ grown on the surface defect site of OCNT via solvothermal treatment and calcination (Fig. S1). Significantly, we select the mole ratio of Ru³⁺ and Co²⁺ to 1: 2 in order

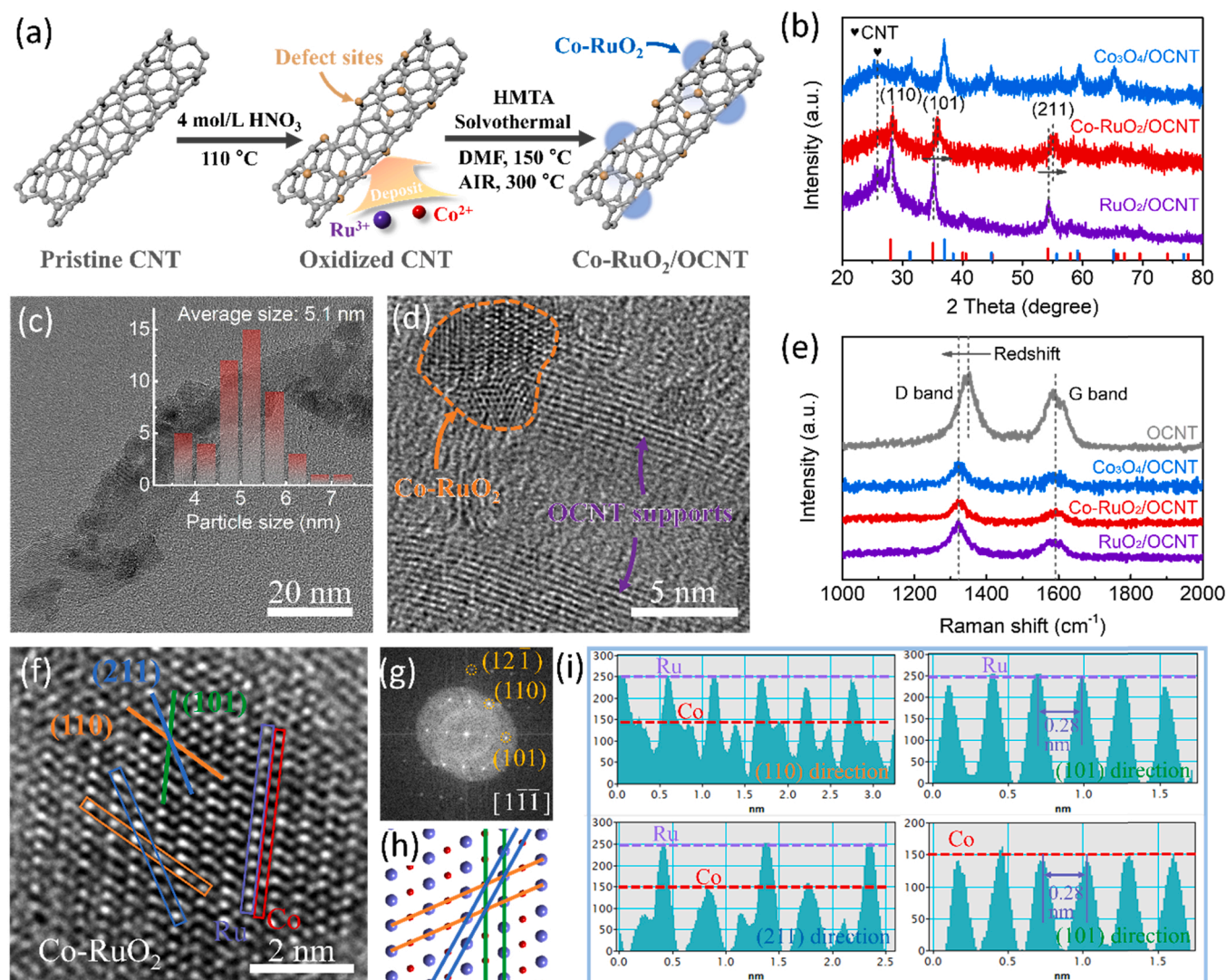


Fig. 1. Structural characterization of Co-RuO₂/OCNT catalyst. (a) Schematic illustration for preparing Co-RuO₂/OCNT; (b) XRD patterns of various catalysts; (c) TEM (the inset exhibits the diameter distribution of Co-doped RuO₂ particle) and (d) HRTEM images of Co-RuO₂/OCNT; (e) Raman scattering spectra of various catalysts; (f) HRTEM image, (g) corresponding FFT image, and (h) atomic structure for the axis of [111] for Co-doped RuO₂ particle, in which the yellow, green, and blue lines represent the (110), (101) and (211) planes respectively; and (i) lattice spacings of (110), (211), and (101) crystal face for the marked areas in (f).

to decrease the mass content of Ru. Compared to OCNT which shows a relatively smooth surface, Co-RuO₂/OCNT behaves in a rough nanofiber morphology by supporting the catalyst layer on the OCNT surface from scanning electron microscopy (SEM) images (Fig. S2). X-ray diffraction (XRD) characterization was further applied to explore the crystal structure of the supported catalyst. As shown in Fig. 1b, the main peaks located at 28.1, 35.0, and 54.1° are attributed to (110), (101), and (211) planes of RuO₂ respectively (JCPDS 00-040-1290) [32], and the peak located at 25.7° is recognized as the characteristic (001) plane of OCNT [33]. Both the Co-RuO₂/OCNT and RuO₂/OCNT show similar diffraction peaks, which indicates that Co atoms are successfully doped into RuO₂/OCNT, even though the molar amount of Co is twice that of Ru. Remarkably, the peak position of (110) plane is not shifted, while the peaks position of (101) and (211) planes are positively shifted about 0.6° after Co ion doping, revealing that Co ion is doped into the specific plane of RuO₂, not random doping. Without adding Ru³⁺ in the precursor solution, only Co₃O₄/OCNT was obtained through the same preparation procedure. For comparison, high and low mass loads of Co-RuO₂ on OCNT were prepared for exploring optimal mass loads (Fig. S3a), and the different amount of Co in RuO₂ were investigated for achieving optimal doping amount (Fig. S3b). When the atomic ratio of Co to Ru is

higher than 3, the obvious diffraction peak of Co₃O₄ appears in the XRD spectrum.

The Co-RuO₂ nanoparticles with an average size of 5.1 nm are evenly anchored on their surface according to transmission electron microscopy (TEM) images in Fig. 1c and Fig. S4. Owing to the abundant defect sites on OCNT supports, the Co-RuO₂ nanoparticles are tightly supported on the OCNT surface via the defect site (Fig. 1d), and the obvious hetero-interface between Co-RuO₂ and OCNT is also clearly observed in Fig. S1. In addition, the D band (sp³ defect carbon) of Co-RuO₂/OCNT, RuO₂/OCNT, and Co₃O₄/OCNT exhibits a negative shift (redshift) about 27 cm⁻¹ compared to OCNT, while the G band (sp² graphite carbon) remains unchanged in Raman spectrum (Fig. 1e), which further indicates that the Co-RuO₂, RuO₂, and Co₃O₄ nanoparticle mainly supports on the defect site of OCNT supports [12,34,35]. Similarly, the C-O bond in OCNT is negatively shifted about 0.1 eV after integrating Co-RuO₂ from high-resolution C 1s XPS spectra in Fig. S5, therefore, the strong chemical interaction between Co-RuO₂ and OCNT can accelerate the electron transfer rate and even restrain the accumulation of Co-RuO₂ during ORR and OER process [36,37]. The high-angle annular dark field scanning transmission electron microscopy (HAADF-STEM) further proves that the Co-RuO₂ (bright nanoparticles) are uniformly anchored

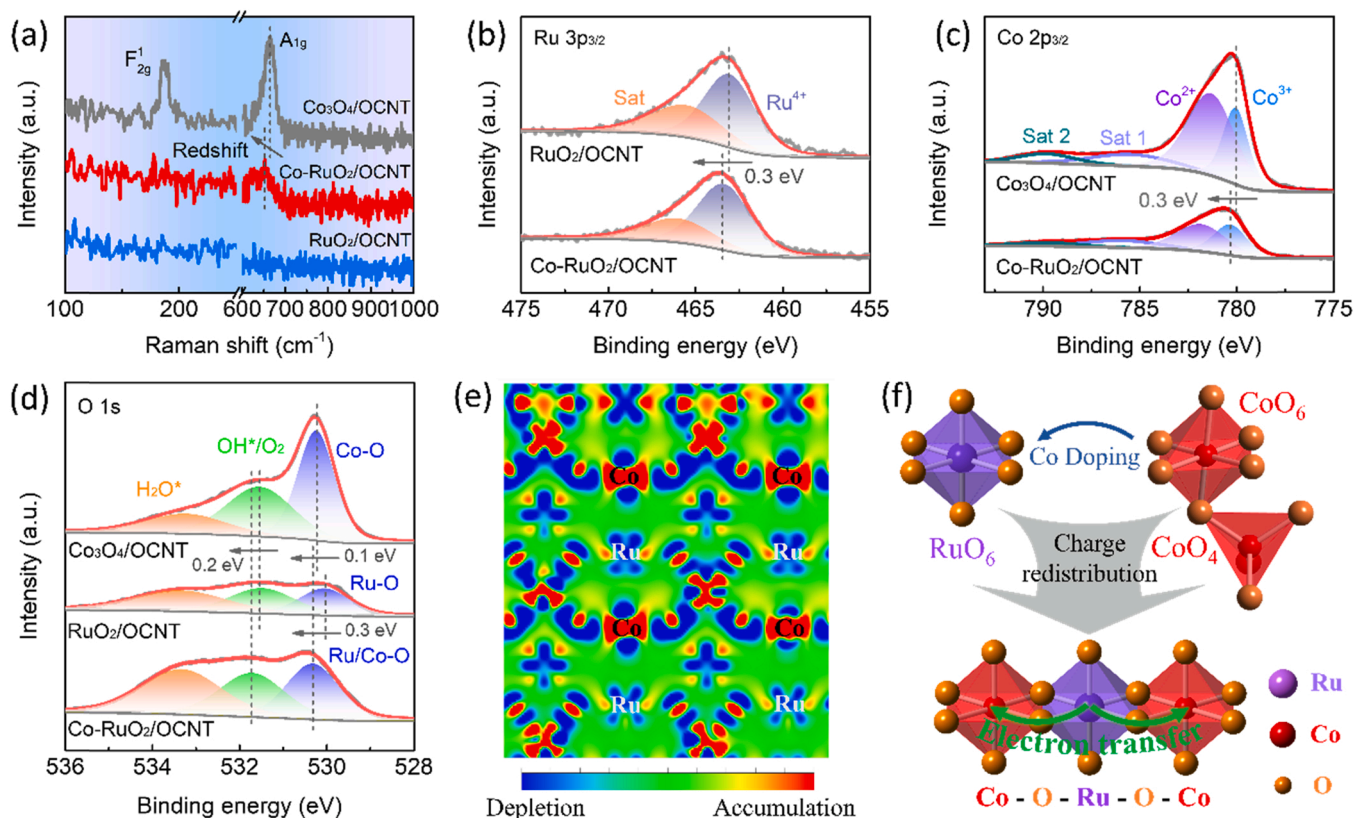


Fig. 2. Electronic structure characterization of Co-RuO₂/OCNT catalyst. (a) Raman scattering spectra of Co-RuO₂/OCNT, RuO₂/OCNT and Co₃O₄/OCNT; High-resolution XPS spectra of (b) Ru 3p for Co-RuO₂/OCNT and RuO₂/OCNT, (c) Co 2p_{3/2} for Co-RuO₂/OCNT and Co₃O₄/OCNT, and (d) O 1s for Co-RuO₂/OCNT, RuO₂/OCNT and Co₃O₄/OCNT; (e) Charge density difference of Co-doped RuO₂ for (001) slice. Charge accumulation and depletion are indicated by red and blue area respectively. The bar scales from -0.1–0.1. (f) Schematic illustration of the electron transfer between Co and Ru atoms in Co-doped RuO₂.

on the OCNT (dark nanowires) surface from energy-dispersive X-ray spectroscopy (EDX) elemental mapping in Fig. S6. The mass load of Co-RuO₂ on OCNT supports is slightly lower than 61% for Co-RuO₂/OCNT (Fig. S7), which approaches the theoretical mass load of 58%. Besides, the atomic fraction of Co atom is about 2.7 times to Ru atom from the corresponding EDX spectrum (Fig. S8), which approaches the molar ratio of added precursor. Therefore, the mass content of Ru in Co-RuO₂/OCNT is about ~15%. High-resolution transmission electron microscopy (HRTEM) is applied to explore the doping site of Co ion. As shown in Fig. 1f, three lattice planes that ascribe to (110), (101), and (211) planes of RuO₂ are clearly observed, meanwhile, a fast Fourier transform (FFT) pattern along the [111] direction supports the tetragonal structure (Fig. 1g). Especially, the atomic brightness along the (101) plane direction is different, in which the bright atom layer represents Ru and the dark atom layer represents Co owing to the different atomic weights (Fig. 1i). Meanwhile, alternate Ru and Co atoms are observed along the (110) and (211) directions. The above observation proves the Co is mainly doped into (101) plane of RuO₂ as depicted by the atomic model along [111] direction in Fig. 1h, which is well consistent with the XRD results. Based on the above discussion, we propose a structural model of Co-RuO₂/OCNT in Fig. S9.

To gain detailed insight into the doping effect of Co ion, we explored the electronic structure information of Co-RuO₂/OCNT, RuO₂/OCNT, and Co₃O₄/OCNT using Raman and X-ray photoelectron spectroscopy (XPS) technology. In Fig. 2a, Co-RuO₂/OCNT exhibits one characteristic peak located at 652 cm⁻¹ while not observed for RuO₂/OCNT, indicating that the peak is attributed to the asymmetric A_{1g} mode of CoO₆ site [38, 39]. Besides, the Raman peak located at 188 cm⁻¹ corresponds to the F_{2g} symmetry of CoO₄ in A site of Co₃O₄ [40,41], while this F_{2g} peak is not observed for Co-RuO₂/OCNT, revealing the Co ion mainly exists in the

form of CoO₆ in Co-RuO₂/OCNT. Moreover, the redshift (about 13 cm⁻¹) of A_{1g} mode is occurred for Co-RuO₂/OCNT owing to electron delocalization that induces shorten of Co-O bond [21,40]. As we previous reports, this redshift phenomenon is caused by the formation of Ru-O-Co bond, especially from the (110) active plane [21]. The Ru-O-Co covalent bond inside the Co-RuO₂/OCNT will induce a charge redistribution effect owing to different electronegativity for Co and Ru ions [42,43], which is further explored by XPS technology. The Ru 3p XPS spectrum encounters a positive shift of 0.3 eV for Ru⁴⁺ after Co doping, indicating the loss of electron for Ru atom after forming the Ru-O-Co bond (Fig. 2b) [20,21]. In addition, the Co 2p XPS spectrum of Co-RuO₂/OCNT and Co₃O₄/OCNT are also presented in Fig. 2c, in which the Co 2p_{3/2} can deconvolute to four peaks including Co³⁺, Co²⁺, and two satellite peaks [44,45]. Significantly, the Co³⁺ is shifted to a low valence state for about 0.3 eV, revealing the Co ion in Co-RuO₂/OCNT serves as the electron acceptor through the Ru-O-Co bond [46]. Oxygen that bridges the Co and Ru ions involves the charge redistribution of the Ru-O-Co bond owing to the orbital overlap of O 2p and M 3d. Fig. 2d depicts the O 1s XPS spectrum of Co-RuO₂/OCNT, RuO₂/OCNT, and Co₃O₄/OCNT. Generally, the O 1s spectrum can deconvolute to three peaks that index to lattice oxygen species (M-O), adsorbed hydroxyl species or oxygen (OH⁺/O₂⁺), and adsorbed water species (H₂O⁺) [47,48]. The binding energy of Ru-O-Co is positively shifted about 0.1 eV and 0.3 eV compared with that of Co-O and Ru-O respectively, which proves the charge redistribution between Ru, O, and Co atoms through the Ru-O-Co bond. Moreover, high binding energy towards OH⁺/O₂⁺ is obtained for Co-RuO₂/OCNT owing to the formation of the Ru-O-Co bond, also named Ru/Co dual-atom site, which is beneficial to ORR and OER performance [49]. The charge density difference analysis is further performed to probe the bias of electron cloud density. As shown in Fig. 2e and S10, the Co atom gained electrons from adjacent Ru atoms through

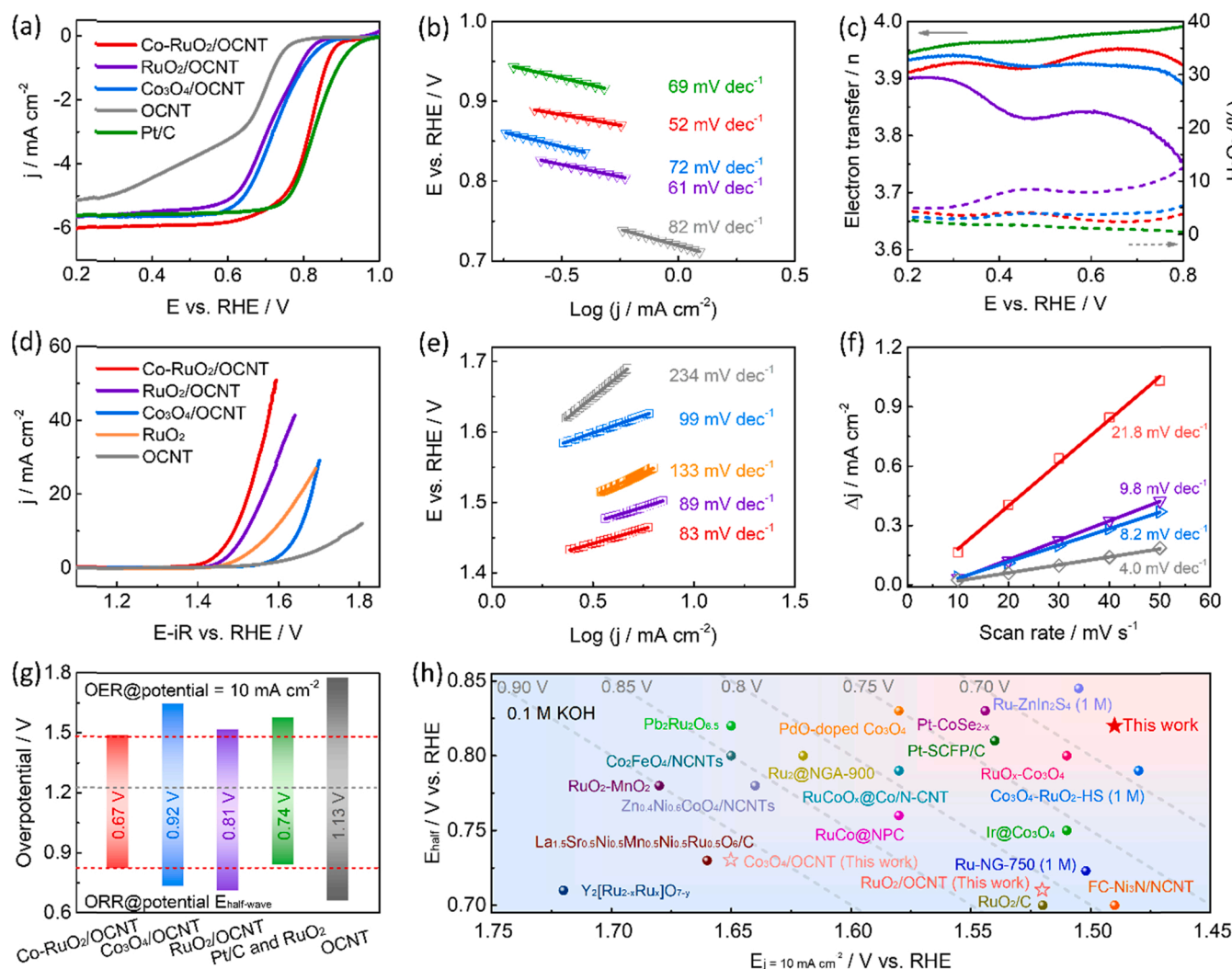


Fig. 3. Electrocatalytic ORR and OER performance in 0.1 M KOH. (a) LSV curves of ORR at a scan rate of 5 mV s⁻¹, (b) corresponding Tafel plots, and (c) electron transfer number and H₂O₂ yield under potential ranging from 0.2 to 0.8 V for Co-RuO₂/OCNT, RuO₂/OCNT, Co₃O₄/OCNT, OCNT, and Pt/C; (d) LSV curves of OER at a scan rate of 5 mV s⁻¹, (e) corresponding Tafel plots, and (f) current densities difference in CV curves at 0.25 V (vs Hg/HgO) versus scan rate for Co-RuO₂/OCNT, RuO₂/OCNT, Co₃O₄/OCNT, OCNT, and RuO₂; (g) The potential gap between ORR and OER for Co-RuO₂/OCNT, RuO₂/OCNT, Co₃O₄/OCNT, OCNT and Pt/C-RuO₂ mixture; (h) The comparison of ORR and OER performance for reported catalysts with this work, in which the 1 M represents the electrolyte concentrations.

the oxygen bridge, in accordance with the XPS results. Therefore, we propose the configuration of Ru/Co dual-atom site with the edge-sharing CoO₆ and RuO₆ octahedron in Co-RuO₂/OCNT to achieve the charge redistribution, even totally converting the CoO₄ tetrahedron in Co₃O₄ into CoO₆ octahedron in RuO₂ (Fig. 2f). Owing to the Co ion being mainly doped into the (101) plane of RuO₂, the Co-RuO₂/OCNT can achieve an abundant Ru/Co dual-atom site with an ordered arrangement inside [50,51].

3.2. Electrochemical activity

Inspired by the unique electronic structure of Ru/Co dual-atom site in Co-RuO₂/OCNT, the electrocatalytic ORR and OER activities were further evaluated in 0.1 M KOH using a conventional three-electrode device, in which the RuO₂/OCNT and Co₃O₄/OCNT were selected as the comparison. The optimal load of Co-RuO₂ and optimal doping amount of Co in Co-RuO₂ were explored first. As shown in Fig. S11, the moderate load of Co-RuO₂ on OCNT support achieve better ORR and OER activities than other high and low loads. In addition, the ORR and OER activities were improved with increasing the Co-doping amount in RuO₂/OCNT before the generation of Co₃O₄ (Fig. S12). After forming

Co₃O₄, ORR and OER catalytic activities of 1.25Co-RuO₂/OCNT were decreased slightly compared to Co-RuO₂/OCNT. Therefore, we select moderate load of Co-RuO₂ on OCNT support and the optimal doping amount of Co in Co-RuO₂ for further exploration. Fig. 3a depicts the typical ORR polarization curves that derive from linear sweep voltammetry (LSV). Co-RuO₂/OCNT delivered a higher half-wave potential of 0.82 V than RuO₂/OCNT with 0.71 V and Co₃O₄/OCNT with 0.73 V, even approaching the benchmark Pt/C with 0.84 V. Moreover, Co-RuO₂/OCNT exhibits the highest limiting diffusion current than other counterparts owing to the abundant accessible catalytic site. The ORR Tafel slope of Co-RuO₂/OCNT is just 52 mV dec⁻¹, obviously lower than that of 61, 72, and 69 mV dec⁻¹ for RuO₂/OCNT, Co₃O₄/OCNT, and Pt/C respectively, implying more favorable ORR kinetics for Ru/Co dual-atom site (Fig. 3b) [52]. Electron transfer number (n) and H₂O₂ yield rate were also collected to further explore the ORR mechanism through rotating ring-disc electrode (RRDE) technology. As shown in Fig. 3c, Co-RuO₂/OCNT can effectively inhibit the H₂O₂ production by less than 5% ranging from 0.2 – 0.8 V compared with RuO₂/OCNT (5% – 15%) and Co₃O₄/OCNT (lower than 5%). The electron transfer number above 3.9 was observed for Co-RuO₂/OCNT, revealing an ideal four-electron pathway for the ORR process [53]. Moreover, the OCNT achieves the

H₂O₂ production to 80%, indicating a two-electron pathway occurred (Fig. S13). Therefore, OCNT supports not being involved in the ORR process, while just offering the electron transfer route. The long-term durability should be also considered for application in the actual device [54]. Co-RuO₂/OCNT exhibits a minor current loss rate of 10.5% at a potential of −0.565 V (vs. RHE) after 10 h, better than that of 25.5% for benchmark Pt/C (Fig. S14).

Subsequently, OER activities of the above catalysts were further obtained for assessing bifunctionality. As shown in Fig. 3d, Co-RuO₂/OCNT only requires a low overpotential of 260 mV to supply a current of 10 mA cm^{−2}, much lower than that of 290, 420, and 350 mV for RuO₂/OCNT, Co₃O₄/OCNT, and RuO₂ respectively, especially at high current density. The OER kinetics is further evaluated by the Tafel slope. Co-RuO₂/OCNT achieves the lowest Tafel slope of 83 mV dec^{−1} compared with RuO₂/OCNT (89 mV dec^{−1}) and Co₃O₄/OCNT (99 mV dec^{−1}), indicating its lower overpotential at higher current density [42]. Furthermore, the electrochemical surface area (ECSA) of catalysts is calculated from cyclic voltammetry (CV) in Fig. S15. The C_{dl} value of Co-RuO₂/OCNT reaches up to 21.8 mF cm^{−2}, which is 2.22, 2.66, and 5.45 times higher than that of RuO₂/OCNT, Co₃O₄/OCNT, and OCNT respectively, revealing that the Ru/CoO₆ dual site can greatly enhance the adsorption capacity for OH ions compared to RuO₆ and CoO₆ single sites (Fig. 3f) [55], which is consistent with the high binding energy of Ru/CoO₆ towards OH* in Fig. 2d. As regards the OER durability, Co-RuO₂/OCNT export a slight increase of 30 mV in potential after 10 h test at 10 mA cm^{−2}, which is obviously lower than that of 70 mV for RuO₂/OCNT after 10 h and 216 mV for RuO₂ after 5 h (Fig. S16). The poor stability of Ru-based electrocatalyst is mainly due to the dissolution of Ru ion at high oxidation potential [21]. We introduced inductively coupled plasma optical emission spectrometer (ICP-OES) test to examine the KOH electrolytes after stability testing of Co-RuO₂/OCNT (Fig. S17a). The content of Ru and Co in the electrolyte was just ~14 and 17 ppb after stability testing, implying that the dissolution of Ru is strongly inhibited after introducing the Co ion. In addition, we systematically characterized the micromorphology and electronic structure of post-electrocatalysis Co-RuO₂/OCNT. No obvious change in the binding energy was observed for Co 2p spectra in Fig. S17b and Ru 3p spectra in Fig. S17c. For O 1s spectra, the peak at 535.9 eV is associated with ether-type oxygen linkages in Nafion [56]. Besides, the other three peaks that index to lattice oxygen species (M-O), adsorbed hydroxyl species or oxygen (OH*/O₂*), and adsorbed water species (H₂O*) are also observed in Fig. S17d. XPS results prove that the electronic structure of Co-RuO₂/OCNT well remains after stability testing. The micromorphology of post-electrocatalysts is further detected by TEM and HRTEM images. As shown in Figs. S17e and S17f, the supported structure of Co-RuO₂/OCNT well remained after the stability test. In addition, the surface reconstruction of the Co-RuO₂ nanoparticle is not observed and the crystal structure of Co-RuO₂ nanoparticle is well preserved after the stability test. The above post-test all confirms that the Co-RuO₂/OCNT has excellent electrochemical stability.

Overall, Co-RuO₂/OCNT can be regarded as an advisable candidate for the air cathode of Zn-air battery considering the above ORR and OER results. The potential gap (ΔE) between the half-wave potential of ORR and overpotential at 10 mA cm^{−2} of OER is a critical parameter to determine the bifunctional activity of electrocatalysts [57]. As shown in Fig. 3g, Co-RuO₂/OCNT achieves an ultralow ΔE value of 0.67 V, which is greatly lower than that of 0.81 and 0.92 V for RuO₂/OCNT and Co₃O₄/OCNT respectively, even surpassing the commercial benchmark Pt/C and RuO₂. Significantly, OCNT shows an ultrahigh ΔE value of 1.15 V, indicating the supported oxide catalysts offer the main ORR and OER active sites. Moreover, we also compare this work to recently reported Ru-based, noble metal-based, Co-based, and N-doped CNT-supported catalysts in Fig. 3h. The Co-RuO₂/OCNT exhibits a lower ΔE value than most of the reported works, such as ruthenium/cobalt compounds and various supported electrocatalysts, strongly confirming the superiority of our work. The detailed parameters of these

bifunctional electrocatalysts are listed in Table S1.

The excellent bifunctional ORR and OER activities of Co-RuO₂/OCNT reveal its potential in replacing the commercial Pt/C and IrO₂ catalysts for the Zn-air battery (ZAB) application. Fig. 4a and S18 show home-made ZAB, with Co-RuO₂/OCNT as the air cathode (loads of 1 mg cm^{−2}), 6 M KOH and 0.2 M ZnCl₂ solution as the electrolyte, and zinc foil as the anode were assembled for further evaluation. Firstly, primary ZABs with Co-RuO₂/OCNT were evaluated, while commercial Pt/C was applied as the counterpart. The Co-RuO₂/OCNT exhibits overlapped discharge polarization curve with Pt/C before 200 mA cm^{−2} (Fig. 4b). More importantly, the peak power density of Co-RuO₂/OCNT (198 mW cm^{−2}) is just slightly lower than that of the benchmark Pt/C catalyst (217 mW cm^{−2}), which is well consistent with ORR results. In addition, the discharge-specific capacity of ZABs was also calculated based on the mass consumption of zinc metal at 20 mA cm^{−2} in Fig. S19. Co-RuO₂/OCNT and Pt/C acquire similar capacities of 790 and 795 mAh g_{Zn}^{−1} respectively (Fig. 4c), while both the full discharge time is about 15 h (Fig. S20a). Meanwhile, the similar energy density of Co-RuO₂/OCNT and Pt/C is also observed in Fig. S20b. Therefore, low-cost Co-RuO₂/OCNT catalyst endows primary ZABs with comparable discharge performance to commercial high-cost Pt/C catalysts.

To test the rechargeability of Co-RuO₂/OCNT in rechargeable ZABs, the discharge/charge performance was further evaluated. As previous OER test, RuO₂/OCNT exhibits lower overpotential and better stability than commercial RuO₂, therefore, we select the mixture of Pt/C and RuO₂/OCNT (Pt/C-RuO₂/OCNT) as the control bifunctional electrocatalyst (Fig. S21). The polarization curves in Fig. 4d reveal that the Co-RuO₂/OCNT requires a low charge/discharge overpotential to achieve constant output current compared with Pt/C-RuO₂/OCNT. The superior rate performance of Co-RuO₂/OCNT is mainly attributed to the construction of highly conductive OCNT supports that tightly anchor the Co-RuO₂ catalyst to ensure ultrafast electron transfer [58]. Furthermore, the cycling performance of Co-RuO₂/OCNT in ZAB device was evaluated by galvanostatic charge-discharge test. As shown in Fig. 4e, the ZAB with Co-RuO₂/OCNT can stably operate for 800 cycles without obvious polarization decay at 10 mA cm^{−2}, while that with Pt/C-RuO₂/OCNT mixture shows sharp degradation in charge/discharge potential gap after 270 cycles. In detail, the charge/discharge potential gap and round-trip efficiency at the first cycle is 0.70 V and 63.7% for Co-RuO₂/OCNT, which approaches to that 0.73 V and 62.9% for Pt/C-RuO₂/OCNT (Fig. 4f), according with the result of polarization curves in Fig. 4d. Significantly, Co-RuO₂/OCNT can maintain the charge/discharge potential gap and round-trip efficiency at 0.80 V and 58.9% respectively after 800 cycles, while that sharply decays to 1.72 V and 34.6% respectively for Pt/C-RuO₂/OCNT after 270 cycles, further verifying the superior cycling performance of Co-RuO₂/OCNT in practical ZABs device. Considering that the cost of Co-RuO₂/OCNT is only one-fifth of that of Pt/C-RuO₂/OCNT mixture (Detail data presented in supporting information), we believe that Co-RuO₂/OCNT can replace benchmark Pt/C-RuO₂/OCNT mixture for rechargeable Zn-air battery. In addition, the Co and Ru ions can be retrieved from the retired power Li-ion battery and spent catalysts, which may further reduce the cost of Co/Ru-based catalyst. More importantly, the Zn-air battery with Co-RuO₂/OCNT also shows better power density, specific capacity, and cycling performance when compared with the recently reported bifunctional electrocatalyst in Table S2. After 800 cycles, the anode surface is covered with black zinc dendrite or dead zinc (Fig. S22), which may reduce the accessibility of electrolyte to fresh zinc, thus affecting the subsequent charge/discharge performance of ZAB [59]. Therefore, the cycling performance decay of rechargeable ZABs with Co-RuO₂/OCNT can be also attributed to the destruction of zinc anode. Finally, as shown in Fig. 4g and S23, three ZABs in series can power an LED screen for 20 h without obvious weakening of brightness when integrating Co-RuO₂/OCNT catalyst, revealing the potential application value for the designed bifunctional electrocatalyst.

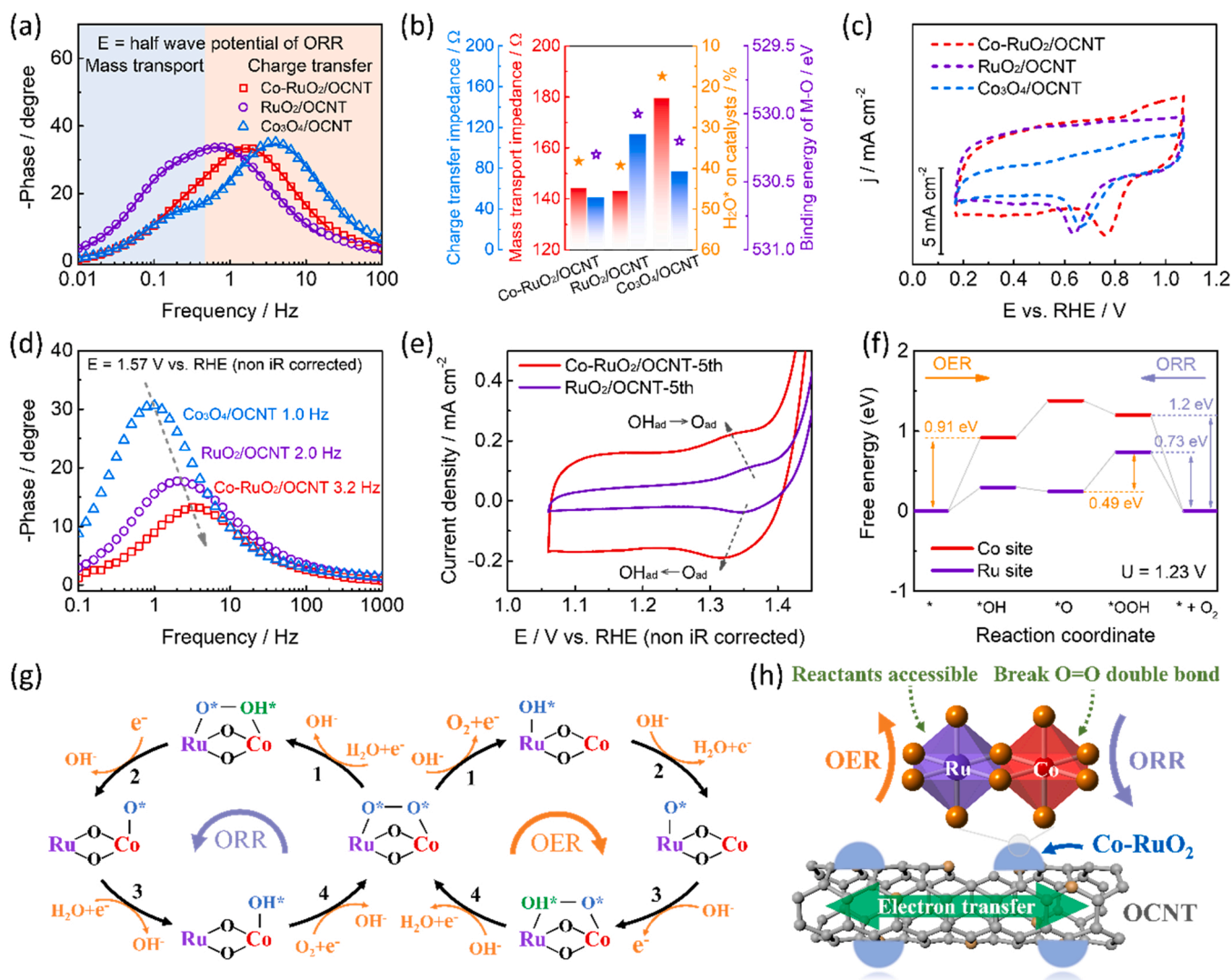


Fig. 5. Electrocatalysis mechanism of ORR and OER. (a) EIS-bode plots at the half-wave potential of ORR, (b) charge transfer and mass transport impedance, and (c) CV curves at potential ranging from -0.7 to 0.2 V vs. Hg/HgO for Co-RuO₂/OCNT, RuO₂/OCNT, and Co₃O₄/OCNT; (d) EIS-bode plots at 1.57 V vs. RHE, (e) CV curves at potential ranging from 1.0 to 1.4 V vs. Hg/HgO for Co-RuO₂/OCNT, RuO₂/OCNT, and Co₃O₄/OCNT; (f) Gibbs free-energy diagram for OER/ORR four steps on the Co site and Ru site for Co-RuO₂ at 1.23 V; (g) ORR and OER mechanism for Co-RuO₂/OCNT; (h) Schematic diagram of mass and electron transfer for Co-RuO₂/OCNT.

et al. [28] The CV area of ORR represents the availability of electrochemically active sites [65]. RuO₂/OCNT exhibits a higher CV area than Co₃O₄/OCNT, even approaching to Co-RuO₂/OCNT, further confirming the function of Ru site in promoting the reactants (oxygen and electrolyte) accessibility during ORR process.

The EIS measurements were further performed to study the OER kinetics of the above catalysts. As expected, Co-RuO₂/OCNT exhibits the lowest charge transfer impedance (R_{ct}) at 1.57 V (vs. RHE, non-iR corrected), revealing its fast reaction kinetics (Fig. S25b) [36]. The corresponding bode plots were further applied to analyze the promoting effect of Ru/Co dual-atom site. As shown in Fig. 5d, the phase peak at the low-frequency region (10^0 – 10^1 Hz) can be attributed to the nonhomogeneous charge distribution that induced by the oxidation of surface catalytic sites [66]. Generally, peak frequency and phase angle are important parameters that reflect the charge transfer kinetics [67]. Co-RuO₂/OCNT achieves the lowest relaxation time based on the highest peak frequency, suggesting that Co-doping can promote the electron transfer rate in its bulk/interface [62]. In addition, the lowest phase angle is also observed for Co-RuO₂/OCNT. This indicates that for Co-RuO₂/OCNT, more electron transfer from active oxygen species to

catalytic sites during PCET steps [68]. Therefore, Co ion in RuO₂ can promote the charge and electron transfer rate respectively in the electrolyte/interface and interface/bulk of catalysts. To better understand the origins of activity, the CV was adopted to explore the redox behavior of catalytic site. As shown in Fig. 5e, the redox peak located at about 1.35 V is assigned to the O_{ad} electro-adsorption ($\text{OH}_{ad} \rightarrow \text{O}_{ad} + \text{H}^+ + \text{e}^-$) on Ru site [69]. We found that this redox peak position shifts to low potential after Co doping, indicating more stable O_{ad} species on Co-RuO₂/OCNT [70]. Differently, Co₃O₄/OCNT shows two redox peaks at about 1.1 and 1.48 V, which are attributed to $\text{Co}^{2+}/\text{Co}^{3+}$ and $\text{Co}^{3+}/\text{Co}^{4+}$ redox pairs respectively (Fig. S26) [21]. Therefore, Ru site in Ru/CoO₆ octahedron serves as the main OER catalytic site, while the doped Co ion can support the PCET steps for promoting the charge and electron transfer rate owing to the charge redistribution effect between Ru and Co atoms.

Furthermore, the density functional theory (DFT) calculation was executed based on the constructed structure models in Fig. S27, while (110) plane is regarded as the active plane [71]. To prove the main active sites during OER and OER, the adsorptions of relevant species (OH^* , O^* , and OOH^*) on Ru and Co sites were respectively performed

for Co-doped RuO₂ in Figs. S28 and S29 [72]. The Gibbs free-energy diagram proves that the OER energy barrier follows the sequence of Ru site (0.49 eV) < Co site (0.91 eV), further confirming that RuO₆ octahedron is the main catalytic site for adsorbing OH* and O* (Fig. 5f and S30) [73]. The formation of OOH* on Ru site is the rate-determining step for OER, while this step is a spontaneous exothermic process on Co site, which is consistent with previous work for the RuO₂/CoO_x system [74]. In addition, the Gibbs free energy for *OOH formation that serves as the rate-determining step of OER is about 0.97 eV for pristine RuO₂ as previous reports [75], which is greatly higher than Co-doped RuO₂ with just 0.49 eV, further confirming the pivotal role of Ru/Co dual-atom site. Similarly, the CoO₆ octahedron serves as the main catalytic site for adsorbing OH* and O* during the ORR process based on the spontaneous exothermic process for converting these two intermediate species. As discussed earlier, the electron-enriched Co site can facilitate the break of O=O double bond that serves as the rate-determining step in ORR [21]. The formation of OOH* on Co site shows a higher energy barrier of 1.2 eV than that on Ru site (0.73 eV), which means that the Ru site can also participate in adsorbing OOH* during ORR process. In addition, H₂O is the main reactant for step 1 of ORR, while abundant adsorbed H₂O* on Ru site serves as the proton donor to promote this step. As reported, the O atom in OOH* shows less negatively charged than O atom in *O or OH* [43], thus the formation of OOH* on the positively charged Ru site requires a high energy barrier during the OER process. The transforming *O to *OOH on Co site is an exothermic process, that can overcome the rate-determining barrier for the Ru site during the OER process. As discussed above, the co-adsorption of OOH* on Ru/Co dual-atom site can promote the ORR and OER activities compared with that merely adsorbed on Ru or Co site, which is also consistent with the electrochemical results. A similar phenomenon reported by Ling et al. reveals that the co-adsorption of OOH* on interfacial Ru/Co dual-atom site to form a nearly quadrilateral structure is the stable configuration in RuO₂/CoO_x hybrid system [74]. Based on the above analysis, we propose the ORR and OER mechanism for the synergistic effect between RuO₆ and CoO₆ sites in Fig. 5g, in which converting the OOH* to O* occurs on Ru site during ORR and O* to OOH* is occurred on Co site during OER based on the model with co-adsorption of OOH* on Ru and Co sites. In addition, the uniform dispersion of Ru/CoO₆ catalytic sites on conductive supports can also ensure fast electron transfer based on the tight hetero-interface between Co-RuO₂ nanoparticle and OCNT (Fig. 5h) [76], while the RuO₆ and CoO₆ octahedron site contribute major OER and ORR activities respectively. This design strategy is directed against the regulation of charge, mass, and electron transfer for constructing superior electrocatalysts for rechargeable ZABs, which can inspire more similar works involving supported catalysts, composite catalysts, and Ru-based catalysts.

4. Conclusions

In summary, a bifunctional electrocatalyst with excess Co-doped RuO₂ nanoparticle supporting an oxidized carbon nanotube (Co-RuO₂/OCNT) was designed through a solvothermal route. The Co ion was mainly doped into the (101) plane of tetragonal RuO₂, thus inducing an abundant Ru/Co dual-atom site in the active (110) surface. As proved, the formation Ru/Co dual site can induce charge redistribution, which can promote the OH*, oxygen, and electrolyte accessibility during OER and ORR, as well as charge and electron transfer rate in the electrolyte/interface and interface/bulk of catalysts respectively. Moreover, the construction of OCNT supports that tightly anchoring Co-RuO₂ nanoparticles via the defect site can promote electron and mass transfer through the whole catalytic layer. As expected, Co-RuO₂/OCNT achieved a low overpotential gap of 0.67 V for ORR/OER and long cycling life of 800 cycles at 10 mA cm⁻² with a charge/discharge gap of 0.70 V for rechargeable Zn-air battery. This work presents new guidance for building efficiently supported electrocatalysts with abundant dual atom catalytic sites for rechargeable ZABs and reveals a synergistic ORR and

OER mechanism between two metal ions through the charge redistribution effect.

CRediT authorship contribution statement

Qian Lu: Data curation, Investigation, Visualization, Writing – original draft preparation. **Xiaohong Zou:** Investigation, Data curation, Methodology, Validation, Software. **Xixi Wang:** Instrumental, Data curation. **Liang An:** Writing – review & editing. **Zongping Shao:** Writing – review & editing, Supervision, Instrumental, Data curation. **Yunfei Bu:** Writing – review & editing, Supervision, Project administration.

Declaration of Competing Interest

The authors declare that they have no known competing financial interests or personal relationships that could have appeared to influence the work reported in this paper.

Data Availability

Data will be made available on request.

Acknowledgements

This work was financially supported by the National Natural Science Foundation of China (22272081), Jiangsu Provincial Specially Appointed Professors Foundation, and Q. Lu thanks the Start-up Foundation for Introducing Talent of NUIST.

Appendix A. Supporting information

Supplementary data associated with this article can be found in the online version at doi:10.1016/j.apcatb.2022.122323.

References

- [1] Y. Zhang, B. Chen, D. Guan, M. Xu, R. Ran, M. Ni, W. Zhou, R. O'Hayre, Z. Shao, Thermal-expansion offset for high-performance fuel cell cathodes, *Nature* 591 (2021) 246, <https://doi.org/10.1038/s41586-021-03264-1>.
- [2] W. Sun, F. Wang, B. Zhang, M. Zhang, V. Kuepers, X. Ji, C. Theile, P. Bieker, K. Xu, C. Wang, M. Winter, A rechargeable zinc-air battery based on zinc peroxide chemistry, *Science* 371 (2021) 46, <https://doi.org/10.1126/science.abb9554>.
- [3] X. Zou, Q. Lu, K. Liao, Z. Shao, Towards practically accessible aprotic Li-air batteries: progress and challenges related to oxygen-permeable membranes and cathodes, *Energy Storage Mater.* 45 (2022) 869–902, <https://doi.org/10.1016/j.ensm.2021.12.031>.
- [4] J. Chen, M. Chen, H. Ma, W. Zhou, X. Xu, Advances and perspectives on separators of aqueous zinc ion batteries, *Energy Rev.* 1 (2022), 100005, <https://doi.org/10.1016/j.enrev.2022.100005>.
- [5] Y. Arafat, M.R. Azhar, Y. Zhong, H.R. Abid, M.O. Tade, Z. Shao, Advances in zeolite imidazolate frameworks (ZIFs) derived bifunctional oxygen electrocatalysts and their application in zinc-air batteries, *Adv. Energy Mater.* 11 (2021) 2100514, <https://doi.org/10.1002/aenm.202100514>.
- [6] P. Tan, B. Chen, H. Xu, H. Zhang, W. Cai, M. Ni, M. Liu, Z. Shao, Flexible Zn- and Li-air batteries: recent advances, challenges, and future perspectives, *Energy Environ. Sci.* 10 (2017) 2056–2080, <https://doi.org/10.1039/C7EE01913K>.
- [7] X. Yu, T. Zhou, J. Ge, C. Wu, Recent advances on the modulation of electrocatalysts based on transition metal nitrides for the rechargeable Zn-air battery, *ACS Mater. Lett.* 2 (2020) 1423–1434, <https://doi.org/10.1021/acsmaterialslett.0c00339>.
- [8] Q. Lu, X. Zou, Y. Bu, Z. Shao, Structural design of supported electrocatalysts for rechargeable Zn-air batteries, *Energy Storage Mater.* 55 (2023) 166–192, <https://doi.org/10.1016/j.ensm.2022.11.046>.
- [9] J. Chen, C. Fan, X. Hu, C. Wang, Z. Huang, G. Fu, J.M. Lee, Y. Tang, Hierarchically porous Co/Co(x)M(y) (M = P, N) as an efficient Mott-Schottky electrocatalyst for oxygen evolution in rechargeable Zn-air batteries, *Small* 15 (2019), e1901518, <https://doi.org/10.1002/sml.201901518>.
- [10] T. Zhou, N. Zhang, C. Wu, Y. Xie, Surface/interface nanoengineering for rechargeable Zn-air batteries, *Energy Environ. Sci.* 13 (2020) 1132–1153, <https://doi.org/10.1039/C9EE03634B>.
- [11] H.B. Tao, J. Zhang, J. Chen, L. Zhang, Y. Xu, J.G. Chen, B. Liu, Revealing energetics of surface oxygen redox from kinetic fingerprint in oxygen electrocatalysis, *J. Am. Chem. Soc.* 141 (2019) 13803–13811, <https://doi.org/10.1021/jacs.9b01834>.
- [12] Q. Lu, X. Zou, Y. Bu, K. Liao, W. Zhou, Z. Shao, A controllable dual interface engineering concept for rational design of efficient bifunctional electrocatalyst for

- zinc-air batteries, *Small* 18 (2022), e2105604, <https://doi.org/10.1002/sml.202105604>.
- [13] M. Luo, W. Sun, B.B. Xu, H. Pan, Y. Jiang, Interface engineering of air electrocatalysts for rechargeable zinc-air batteries, *Adv. Energy Mater.* 11 (2021) 2002762, <https://doi.org/10.1002/aenm.202002762>.
 - [14] C. Guo, Y. Zheng, J. Ran, F. Xie, M. Jaroniec, S.Z. Qiao, Engineering high-energy interfacial structures for high-performance oxygen-involving electrocatalysis, *Angew. Chem. Int. Ed.* 56 (2017) 8539–8543, <https://doi.org/10.1002/anie.201701531>.
 - [15] X. Zhuang, Y. Zhou, Z. Jiang, X. Yao, X.-Y. Yu, Synergetic electronic modulation and nanostructure engineering of heterostructured $\text{RuO}_2/\text{Co}_3\text{O}_4$ as advanced bifunctional electrocatalyst for zinc-air batteries, *J. Mater. Chem. A* 9 (2021) 26669–26675, <https://doi.org/10.1039/D1TA09278B>.
 - [16] Y. Gao, D. Zheng, Q. Li, W. Xiao, T. Ma, Y. Fu, Z. Wu, L. Wang, 3D Co_3O_4 - RuO_2 hollow spheres with abundant interfaces as advanced trifunctional electrocatalyst for water-splitting and flexible Zn-air battery, *Adv. Mater.* 32 (2022) 2203206, <https://doi.org/10.1002/adfm.202203206>.
 - [17] A. Yu, M.H. Kim, C. Lee, Y. Lee, Structural transformation between rutile and spinel crystal lattices in Ru-Co binary oxide nanotubes: enhanced electron transfer kinetics for the oxygen evolution reaction, *Nanoscale* 13 (2021) 13776–13785, <https://doi.org/10.1039/D1NR02244J>.
 - [18] Y. Dai, J. Yu, Z. Zhang, S. Zhai, C. Cheng, S. Zhao, P. Tan, Z. Shao, M. Ni, Regulating the interfacial electron density of $\text{La}_{0.8}\text{Sr}_{0.2}\text{Mn}_{0.5}\text{Co}_{0.5}\text{O}_{3-x}/\text{RuO}_x$ for efficient and low-cost bifunctional oxygen electrocatalysts and rechargeable Zn-air batteries, *ACS Appl. Mater. Interfaces* 13 (2021) 61098–61106, <https://doi.org/10.1021/acsami.1c18081>.
 - [19] C. Huang, Q. Ji, H. Zhang, Y. Wang, S. Wang, X. Liu, Y. Guo, C. Zhang, Ru-incorporated Co_3O_4 nanoparticles from self-sacrificial ZIF-67 template as efficient bifunctional electrocatalysts for rechargeable metal-air battery, *J. Colloid Interface Sci.* 606 (2022) 654–665, <https://doi.org/10.1016/j.jcis.2021.08.046>.
 - [20] C. Zhou, S. Zhao, H. Meng, Y. Han, Q. Jiang, B. Wang, X. Shi, W. Zhang, L. Zhang, R. Zhang, RuCoO_x nanofoam as a high-performance trifunctional electrocatalyst for rechargeable zinc-air batteries and water splitting, *Nano Lett.* 21 (2021) 9633–9641, <https://doi.org/10.1021/acs.nanolett.1c03407>.
 - [21] Q. Lu, Y. Guo, P. Mao, K. Liao, X. Zou, J. Dai, P. Tan, R. Ran, W. Zhou, M. Ni, Z. Shao, Rich atomic interfaces between sub-1 nm RuO_x clusters and porous Co_3O_4 nanosheets boost oxygen electrocatalysis bifunctionality for advanced Zn-air batteries, *Energy Storage Mater.* 32 (2020) 20–29, <https://doi.org/10.1016/j.ensm.2020.06.015>.
 - [22] B. Guo, R. Ma, Z. Li, S. Guo, J. Luo, M. Yang, Q. Liu, T. Thomas, J. Wang, Hierarchical N-doped porous carbons for Zn-air batteries and supercapacitors, *Nano-Micro Lett.* 12 (2020) 20, <https://doi.org/10.1007/s40820-019-0364-z>.
 - [23] Y. Jiang, Y.-P. Deng, R. Liang, J. Fu, D. Luo, G. Liu, J. Li, Z. Zhang, Y. Hu, Z. Chen, Multidimensional ordered bifunctional air electrode enables flash reactants shuttling for high-energy flexible Zn-air batteries, *Adv. Energy Mater.* 9 (2019) 1909911, <https://doi.org/10.1002/aenm.201909911>.
 - [24] Y. Zhang, Y.-P. Deng, J. Wang, Y. Jiang, G. Cui, L. Shui, A. Yu, X. Wang, Z. Chen, Recent progress on flexible Zn-air batteries, *Energy Storage Mater.* 35 (2021) 538–549, <https://doi.org/10.1016/j.ensm.2020.09.008>.
 - [25] G. Fu, J. Wang, Y. Chen, Y. Liu, Y. Tang, J.B. Goodenough, J.-M. Lee, Exploring indium-based ternary thiospinel as conceivable high-potential air-cathode for rechargeable Zn-air batteries, *Adv. Energy Mater.* 8 (2018) 1802263, <https://doi.org/10.1002/aenm.201802263>.
 - [26] S. Li, C. Cheng, X. Zhao, J. Schmidt, A. Thomas, Active salt/silica-templated 2D mesoporous FeCo-Nx -carbon as bifunctional oxygen electrodes for zinc-air batteries, *Angew. Chem., Int. Ed.* 57 (2018) 1856–1862, <https://doi.org/10.1002/anie.201710852>.
 - [27] H. Wang, J. Li, K. Li, Y. Lin, J. Chen, L. Gao, V. Nicolosi, X. Xiao, J.M. Lee, Transition metal nitrides for electrochemical energy applications, *Chem. Soc. Rev.* 50 (2021) 1354–1390, <https://doi.org/10.1039/D0CS00415D>.
 - [28] W. Cheng, X.F. Lu, D. Luan, X.W.D. Lou, NiMn-based bimetal-organic framework nanosheets supported on multi-channel carbon fibers for efficient oxygen electrocatalysis, *Angew. Chem., Int. Ed.* 59 (2020) 18234–18239, <https://doi.org/10.1002/anie.202008129>.
 - [29] R. Ma, G. Lin, Q. Ju, W. Tang, G. Chen, Z. Chen, Q. Liu, M. Yang, Y. Lu, J. Wang, Edge-sited Fe-N_4 atomic species improve oxygen reduction activity via boosting O_2 dissociation, *Appl. Catal. B: Environ.* 265 (2020), 118593, <https://doi.org/10.1016/j.apcatb.2020.118593>.
 - [30] Y. Jiang, Y.-P. Deng, J. Fu, D.U. Lee, R. Liang, Z.P. Cano, Y. Liu, Z. Bai, S. Hwang, L. Yang, D. Su, W. Chu, Z. Chen, Interpenetrating triphase cobalt-based nanocomposites as efficient bifunctional oxygen electrocatalysts for long-lasting rechargeable Zn-air batteries, *Adv. Energy Mater.* 8 (2018) 1702900, <https://doi.org/10.1002/aenm.201702900>.
 - [31] G. Fu, Y. Wang, Y. Tang, K. Zhou, J.B. Goodenough, J.-M. Lee, Superior oxygen electrocatalysis on nickel indium thiospinel for rechargeable Zn-air batteries, *ACS Mater. Lett.* 1 (2019) 123–131, <https://doi.org/10.1021/acsmaterialslett.9b00093>.
 - [32] Y. Qiu, Y. Rao, Y. Zheng, H. Hu, W. Zhang, X. Guo, Activating ruthenium dioxide via compressive strain achieving efficient multifunctional electrocatalysis for Zn-air batteries and overall water splitting, *InfoMat* 4 (2022), e12326, <https://doi.org/10.1002/inf2.12326>.
 - [33] Q. Lu, X. Zou, K. Liao, R. Ran, W. Zhou, M. Ni, Z. Shao, Direct growth of ordered N-doped carbon nanotube arrays on carbon fiber cloth as a free-standing and binder-free air electrode for flexible quasi-solid-state rechargeable Zn-Air Batteries, *Carbon Energy* (2020) 461–471, <https://doi.org/10.1002/cey2.50>.
 - [34] J. Zou, Y. Lin, S. Wu, Y. Zhong, C. Yang, Molybdenum Dioxide Nanoparticles Anchored on Nitrogen-Doped Carbon Nanotubes as Oxidative Desulfurization Catalysts: Role of Electron Transfer in Activity and Reusability, *Adv. Funct. Mater.* 31 (2021) 2100442, <https://doi.org/10.1002/adfm.202100442>.
 - [35] Y. Wang, M. Wu, J. Li, H. Huang, J. Qiao, In situ growth of CoP nanoparticles anchored on (N,P) co-doped porous carbon engineered by MOFs as advanced bifunctional oxygen catalyst for rechargeable Zn-air battery, *J. Mater. Chem. A* 8 (2020) 19043–19049, <https://doi.org/10.1039/D0TA06435A>.
 - [36] Q. Lu, X. Zou, C. Wang, K. Liao, P. Tan, R. Ran, W. Zhou, S.-G. Ni, Z. Shao, Tailoring charge and mass transport in cation/anion-codoped $\text{Ni}_3\text{N}/\text{N}$ -doped CNT integrated electrode toward rapid oxygen evolution for fast-charging zinc-air batteries, *Energy Storage Mater.* 39 (2021) 11–20, <https://doi.org/10.1016/j.ensm.2021.04.013>.
 - [37] K. Huang, R. Wang, S. Zhao, P. Du, H. Wang, H. Wei, Y. Long, B. Deng, M. Lei, B. Ge, H. Gou, R. Zhang, H. Wu, Atomic species derived CoO_x clusters on nitrogen doped mesoporous carbon as advanced bifunctional electro-catalysts for Zn-air battery, *Energy Storage Mater.* 29 (2020) 156–162, <https://doi.org/10.1016/j.ensm.2020.03.026>.
 - [38] Q. Lu, J. Yu, X. Zou, K. Liao, P. Tan, W. Zhou, M. Ni, Z. Shao, Self-catalyzed growth of Co, N-codoped CNTs on carbon-encased CoS_x surface: a noble-metal-free bifunctional oxygen electrocatalyst for flexible solid Zn-air batteries, *Adv. Funct. Mater.* 29 (2019) 1904481, <https://doi.org/10.1002/adfm.201904481>.
 - [39] X. He, X. Yi, F. Yin, B. Chen, G. Li, H. Yin, Less active CeO_2 regulating bifunctional oxygen electrocatalytic activity of $\text{Co}_3\text{O}_4/\text{N}$ -doped carbon for Zn-air batteries, *J. Mater. Chem. A* 7 (2019) 6753–6765, <https://doi.org/10.1039/C9TA00302A>.
 - [40] S.-H. Hsu, S.-F. Hung, H.-Y. Wang, F.-X. Xiao, L. Zhang, H. Yang, H.M. Chen, J.-M. Lee, B. Liu, Tuning the Electronic Spin State of Catalysts by Strain Control for Highly Efficient Water Electrolysis, *Small Methods* 2 (2018) 1800001, <https://doi.org/10.1002/smt.201800001>.
 - [41] Z. Wang, J. Huang, L. Wang, Y. Liu, W. Liu, S. Zhao, Z.-Q. Liu, Cation-tuning induced d-band center modulation on Co-based spinel oxide for oxygen reduction/evolution reaction, *Angew. Chem. Int. Ed.* 61 (2022), 202114696, <https://doi.org/10.1002/anie.202114696>.
 - [42] J. Dai, Y. Zhu, Y. Yin, H.A. Tahini, D. Guan, F. Dong, Q. Lu, S.C. Smith, X. Zhang, H. Wang, W. Zhou, Z. Shao, Super-exchange interaction induced overall optimization in ferromagnetic perovskite oxides enables ultrafast water oxidation, *Small* 15 (2019), e1903120, <https://doi.org/10.1002/sml.201903120>.
 - [43] H. Su, S. Song, Y. Gao, N. Li, Y. Fu, L. Ge, W. Song, J. Liu, T. Ma, In situ electronic redistribution tuning of NiCo_2S_4 nanosheets for enhanced electrocatalysis, *Adv. Funct. Mater.* 32 (2021) 2109731, <https://doi.org/10.1002/adfm.202109731>.
 - [44] N.-F. Yu, C. Wu, W. Huang, Y.-H. Chen, D.-Q. Ruan, K.-L. Bao, H. Chen, Y. Zhang, Y. Zhu, Q.-H. Huang, W.-H. Lai, Y.-X. Wang, H.-G. Liao, S.-G. Ni, Y.-P. Wu, J. Wang, Highly efficient $\text{Co}_3\text{O}_4/\text{Co}/\text{N}$ -doped carbon bifunctional oxygen electrocatalysts for long life rechargeable Zn-air batteries, *Nano Energy* 77 (2020), 105200, <https://doi.org/10.1016/j.nanoen.2020.105200>.
 - [45] H. Liang, F. Meng, M. Caban-Acevedo, L. Li, A. Forticaux, L. Xiu, Z. Wang, S. Jin, Hydrothermal continuous flow synthesis and exfoliation of NiCo layered double hydroxide nanosheets for enhanced oxygen evolution catalysis, *Nano Lett.* 15 (2015) 1421–1427, <https://doi.org/10.1021/nl504872s>.
 - [46] X.R. Wang, J.Y. Liu, Z.W. Liu, W.C. Wang, J. Luo, X.-P. Han, X.W. Du, S.Z. Qiao, J. Yang, Identifying the key role of pyridinic-N-Co bonding in synergistic electrocatalysis for reversible ORR/OER, *Adv. Mater.* 30 (2018), e1800005, <https://doi.org/10.1002/adma.201800005>.
 - [47] X. Wang, J. Sunarso, Q. Lu, Z. Zhou, J. Dai, D. Guan, W. Zhou, Z. Shao, High-performance platinum-perovskite composite bifunctional oxygen electrocatalyst for rechargeable Zn-air battery, *Adv. Energy Mater.* 10 (2020) 1903271, <https://doi.org/10.1002/aenm.201903271>.
 - [48] X. Han, G. He, Y. He, J. Zhang, X. Zheng, L. Li, C. Zhong, W. Hu, Y. Deng, T.-Y. Ma, Engineering catalytic active sites on cobalt oxide surface for enhanced oxygen electrocatalysis, *Adv. Energy Mater.* 8 (2018) 1702222, <https://doi.org/10.1002/aenm.201702222>.
 - [49] Y. Yan, S. Liang, X. Wang, M. Zhang, S.-M. Hao, X. Cui, Z. Li, Z. Lin, Robust wrinkled $\text{MoS}_2/\text{N-C}$ bifunctional electrocatalysts interfaced with single Fe atoms for wearable zinc-air batteries, *Proc. Natl. Acad. Sci. USA* 118 (2021), 2110036118, <https://doi.org/10.1073/pnas.2110036118>.
 - [50] S. Chen, H. Huang, P. Jiang, K. Yang, J. Diao, S. Gong, S. Liu, M. Huang, H. Wang, Q. Chen, Mn-doped RuO_2 nanocrystals as highly active electrocatalysts for enhanced oxygen evolution in acidic media, *ACS Catal.* 10 (2019) 1152–1160, <https://doi.org/10.1021/acscatal.9b04922>.
 - [51] C. Zhou, X. Chen, S. Liu, Y. Han, H. Meng, Q. Jiang, S. Zhao, F. Wei, J. Sun, T. Tan, R. Zhang, Superdurable bifunctional oxygen electrocatalyst for high-performance zinc-air batteries, *J. Am. Chem. Soc.* 144 (2022) 2694–2704, <https://doi.org/10.1021/jacs.1c11675>.
 - [52] L. Wei, H.E. Karahan, S. Zhai, H. Liu, X. Chen, Z. Zhou, Y. Lei, Z. Liu, Y. Chen, Amorphous bimetallic oxide-graphene hybrids as bifunctional oxygen electrocatalysts for rechargeable Zn-air batteries, *Adv. Mater.* 29 (2017) 1701410, <https://doi.org/10.1002/adma.201701410>.
 - [53] V. Jose, J.M.V. Nsanzimana, H. Hu, J. Choi, X. Wang, J.M. Lee, Highly efficient oxygen reduction reaction activity of N-doped carbon-cobalt boride heterointerfaces, *Adv. Energy Mater.* 11 (2021) 2100157, <https://doi.org/10.1002/aenm.202100157>.
 - [54] C.-Y. Su, H. Cheng, W. Li, Z.-Q. Liu, N. Li, Z. Hou, F.-Q. Bai, H.-X. Zhang, T.-Y. Ma, Atomic modulation of FeCo-nitrogen-carbon bifunctional oxygen electrodes for rechargeable and flexible all-solid-state zinc-air battery, *Adv. Energy Mater.* 7 (2017) 1602420, <https://doi.org/10.1002/aenm.201602420>.
 - [55] Z. Xiao, Y.-C. Huang, C.L. Dong, C. Xie, Z. Liu, S. Du, W. Chen, D. Yan, L. Tao, Z. Shu, G. Zhang, H. Duan, Y. Wang, Y. Zou, R. Chen, S. Wang, Operando identification of the dynamic behavior of oxygen vacancy-rich Co_3O_4 for oxygen

- evolution reaction, *J. Am. Chem. Soc.* 142 (2020) 12087–12095, <https://doi.org/10.1021/jacs.0c00257>.
- [56] D. Susac, M. Kono, K.C. Wong, K.A.R. Mitchell, XPS study of interfaces in a two-layer light-emitting diode made from PPV and Nafion with ionically exchanged Ru (bpy)₃²⁺, *Appl. Surf. Sci.* 174 (2001) 43–50, [https://doi.org/10.1016/S0169-4332\(01\)00026-5](https://doi.org/10.1016/S0169-4332(01)00026-5).
- [57] C.-X. Zhao, J.-N. Liu, J. Wang, D. Ren, B.-Q. Li, Q. Zhang, Recent advances of noble-metal-free bifunctional oxygen reduction and evolution electrocatalysts, *Chem. Soc. Rev.* 50 (2021) 7745–7778, <https://doi.org/10.1039/D1CS00135C>.
- [58] G. Fu, X. Yan, Y. Chen, L. Xu, D. Sun, J.M. Lee, Y. Tang, Boosting bifunctional oxygen electrocatalysis with 3d graphene aerogel-supported Ni/MnO particles, *Adv. Mater.* 30 (2018) 201704609, <https://doi.org/10.1002/adma.201704609>.
- [59] J. Hao, X. Li, S. Zhang, F. Yang, X. Zeng, S. Zhang, G. Bo, C. Wang, Z. Guo, Designing dendrite-free zinc anodes for advanced aqueous zinc batteries, *Adv. Funct. Mater.* 30 (2020) 2001263, <https://doi.org/10.1002/adfm.202001263>.
- [60] R.K. Singh, R. Devivaraprasad, T. Kar, A. Chakraborty, M. Neergat, Electrochemical impedance spectroscopy of oxygen reduction reaction (ORR) in a rotating disk electrode configuration: effect of ionomer content and carbon-support, *J. Electrochem. Soc.* 162 (2015) F489–F498, <https://doi.org/10.1149/2.0141506jes>.
- [61] S. Roy, S. Mari, M.K. Sai, S.C. Sarma, S. Sarkar, S.C. Peter, Highly efficient bifunctional oxygen reduction/evolution activity of a non-precious nanocomposite derived from a tetrazine-COF, *Nanoscale* 12 (2020) 22718–22734, <https://doi.org/10.1039/D0NR05337F>.
- [62] Y. Du, D. Liu, T. Li, Y. Yan, Y. Liang, S. Yan, Z. Zou, A phase transformation-free redox couple mediated electrocatalytic oxygen evolution reaction, *Appl. Catal. B: Environ.* 306 (2022), 121146, <https://doi.org/10.1016/j.apcatb.2022.121146>.
- [63] C. Li, X. Han, F. Cheng, Y. Hu, C. Chen, J. Chen, Phase and composition controllable synthesis of cobalt manganese spinel nanoparticles towards efficient oxygen electrocatalysis, *Nat. Commun.* 6 (2015) 7345, <https://doi.org/10.1038/ncomms8345>.
- [64] M. Wang, B. Han, J. Deng, Y. Jiang, M. Zhou, M. Lucero, Y. Wang, Y. Chen, Z. Yang, A.T. N'Diaye, Q. Wang, Z.J. Xu, Z. Feng, Influence of Fe substitution into LaCoO₃ electrocatalysts on oxygen-reduction activity, *ACS Appl. Mater. Interfaces* 11 (2019) 5682–5686, <https://doi.org/10.1021/acsami.8b20780>.
- [65] F. Razmjooei, K.P. Singh, M.Y. Song, J.-S. Yu, Enhanced electrocatalytic activity due to additional phosphorous doping in nitrogen and sulfur-doped graphene: a comprehensive study, *Carbon* 78 (2014) 257–267, <https://doi.org/10.1016/j.carbon.2014.07.002>.
- [66] H.Y. Wang, S.F. Hung, H.Y. Chen, T.S. Chan, H.M. Chen, B. Liu, In operando identification of geometrical-site-dependent water oxidation activity of spinel Co₃O₄, *J. Am. Chem. Soc.* 138 (2016) 36–39, <https://doi.org/10.1021/jacs.5b10525>.
- [67] N. Zhang, Y. Hu, L. An, Q. Li, J. Yin, J. Li, R. Yang, M. Lu, S. Zhang, P. Xi, C.-H. Yan, Surface activation and Ni-S stabilization in NiO/NiS₂ for efficient oxygen evolution reaction, *Angew. Chem. Int. Ed.* 61 (2022), e202207217, <https://doi.org/10.1002/anie.202207217>.
- [68] C. Xie, W. Chen, S. Du, D. Yan, Y. Zhang, J. Chen, B. Liu, S. Wang, In-situ phase transition of WO₃ boosting electron and hydrogen transfer for enhancing hydrogen evolution on Pt, *Nano Energy* 71 (2020), 104653, <https://doi.org/10.1016/j.nanoen.2020.104653>.
- [69] P. Adiga, W. Nunn, C. Wong, A.K. Manjeshwar, S. Nair, B. Jalan, K.A. Stoerzinger, Breaking OER and CER scaling relations via strain and its relaxation in RuO₂ (101), *Mater. Today Energy* 28 (2022), 101087, <https://doi.org/10.1016/j.mtener.2022.101087>.
- [70] B. Hu, D.-Y. Kuo, H. Paik, D.G. Schlom, J. Suntivich, Enthalpy and entropy of oxygen electroadsorption on RuO₂(110) in alkaline media, *J. Chem. Phys.* 152 (2020), 094704, <https://doi.org/10.1063/1.5139049>.
- [71] J. He, W. Li, P. Xu, J. Sun, Tuning electron correlations of RuO₂ by co-doping of Mo and Ce for boosting electrocatalytic water oxidation in acidic media, *Appl. Catal. B: Environ.* 298 (2021), 120528, <https://doi.org/10.1016/j.apcatb.2021.120528>.
- [72] X. Hu, Y. Chen, M. Zhang, G. Fu, D. Sun, J.-M. Lee, Y. Tang, Alveolate porous carbon aerogels supported Co₉S₈ derived from a novel hybrid hydrogel for bifunctional oxygen electrocatalysis, *Carbon* 144 (2019) 557–566, <https://doi.org/10.1016/j.carbon.2018.12.099>.
- [73] V. Jose, H. Hu, E. Edison, W. Manalastas Jr., H. Ren, P. Kidkhunthod, S. Sreejith, A. Jayakumar, J.M.V. Nsanzimana, M. Srinivasan, J. Choi, J.M. Lee, Modulation of single atomic Co and Fe sites on hollow carbon nanospheres as oxygen electrodes for rechargeable Zn-air batteries, *Small Methods* 5 (2021), e2000751, <https://doi.org/10.1002/smt.202000751>.
- [74] K. Du, L. Zhang, J. Shan, J. Guo, J. Mao, C.C. Yang, C.H. Wang, Z. Hu, T. Ling, Interface engineering breaks both stability and activity limits of RuO₂ for sustainable water oxidation, *Nat. Commun.* 13 (2022) 5448, <https://doi.org/10.1038/s41467-022-33150-x>.
- [75] K. Shah, R. Dai, M. Mateen, Z. Hassan, Z. Zhuang, C. Liu, M. Israr, W.-C. Cheong, B. Hu, R. Tu, C. Zhang, X. Chen, Q. Peng, C. Chen, Y. Li, Cobalt single atom incorporated in ruthenium oxide sphere: a robust bifunctional electrocatalyst for HER and OER, *Angew. Chem. Int. Ed.* 61 (2022), e202114951, <https://doi.org/10.1002/ange.202114951>.
- [76] C.X. Zhao, J.N. Liu, J. Wang, D. Ren, J. Yu, X. Chen, B.Q. Li, Q. Zhang, A. DeltaE, = 0.63 V bifunctional oxygen electrocatalyst enables high-rate and long-cycling zinc-air batteries, *Adv. Mater.* 33 (2021), e2008606, <https://doi.org/10.1002/adma.202008606>.